Research Square

Preprints are preliminary reports that have not undergone peer review.
They should not be considered conclusive, used to inform clinical practice,
or referenced by the media as validated information.

I ∝ √V characteristic resulting from a Fermi pinning region in polysilicon nanowire Schottky-contacted resistors

Fouad DEMAMI

f.demami@uiz.ac.ma

Université Ibn Zohr

Akram SEDKI

Université Ibn Zohr

El Hanafi Arjdal

Université Ibn Zohr

Mustapha Elyaqouti

Université Ibn Zohr

El Mehdi Mellouli

Sidi Mohamed Ben Abdellah University

Mohamed Selmouni

Brussels Management School

Ahmed Sali

Sidi Mohamed Ben Abdellah University

Research Article

Keywords: Density of states, Fermi pinning, modelling, nanowire, polysilicon, Schottky contact

Posted Date: October 8th, 2026

DOI: https://doi.org/10.21203/rs.3.rs-10963584/v1

License: This work is licensed under a Creative Commons Attribution 4.0 International License.
Read Full License

Additional Declarations: No competing interests reported.

$I \propto \sqrt{V}$ characteristic resulting from a Fermi pinning region in polysilicon nanowire Schottky-contacted resistors

Fouad Demami[1], Akram Sedki[1], El Hanafi Arjdal[1], Mustapha Elyaqouti[1], El Mehdi Mellouli[2], Mohamed Selmouni[3] and Ahmed Sali[4]

1 Faculty of Sciences, Ibnou Zohr University, Morocco

2 School of Applied Sciences, Sidi Mohamed Ben Abdellah University, Fez, Morocco

3 ICHEC Brussels Management School, Brussels, Belgium

4 Faculty of Sciences, Sidi Mohamed Ben Abdellah University, Fez, Morocco

Corresponding author: Fouad DEMAMI, email: f.demami@uiz.ac.ma

Abstract

Herein, we present an analytical formulation for the current-voltage characteristic of an undoped polycrystalline silicon nanowire Schottky-contacted resistor. This type of nanowire is characterised by high defect density, which is modelled using a double-exponential density of states (DOS) describing both band-tail states and deep states within the bandgap for acceptor and donor traps. At equilibrium, the potential profile reveals an electrostatic screening effect: perturbation induced by the contact is attenuated by the trapped charge over a characteristic screening length, beyond which the potential stabilises to a typical value determined by the DOS parameters. Out of equilibrium, a Fermi pinning region forms near the metal/polycrystalline silicon nanowire interface, which is distinct from depletion regions observed in classical Schottky junctions. This Fermi pinning region exhibits a quasi-frozen trap occupancy and a free-hole concentration around the intrinsic concentration. Beyond this region, quasi-neutrality is restored, with a residual electric field deep in the nanowire ensuring the drift of free holes. The model shows that this field, proportional to the square root of the voltage, is an attenuated replica of the field at the metal/polycrystalline silicon nanowire interface transmitted through the Fermi pinning region and screening region into the core of the nanowire. Based on the drift-diffusion equation, the current-voltage characteristic exhibits a distinctive dependence of the form $I \propto \sqrt{V}$. The developed analytical expressions are quantitatively supported by numerical simulations.

Keywords: Density of states, Fermi pinning, modelling, nanowire, polysilicon, Schottky contact.

1. Introduction

Polycrystalline silicon nanowires (poly-SiNWs) are promising candidates for very-small-scale electronic devices. Their electrical properties [1], [2], compatibility with industrial fabrication processes for electronic devices, and ease of integration make them particularly attractive for devices such as field-effect transistors [3], [4], micro/nanoelectromechanical systems (MEMS/NEMS) [5], [6] and chemical or biological sensors [7], [8], whose sensitivity to surrounding chemical species is now well established. Unlike their monocrystalline counterparts, poly-SiNWs are characterised by a highly disordered microstructure—comprising grain boundaries, dangling bonds, and lattice distortions—which generates a high density of localised states within bandgaps [9], [10], [11]. By trapping free carriers, these states lead to qualitatively different transports compared with doped crystalline semiconductors, in which conduction is governed by fully ionised shallow impurities.

In addition to field-effect architectures, poly-SiNWs are employed in a resistive two-terminal configuration, in which a wire in simple contact with two metal electrodes forms a remarkably simple fabrication device [7], [12]. While this simplicity is attractive for sensing, this configuration makes metal/semiconductor junctions responsible for electrical behaviour, as these interfaces define current–voltage characteristic. However, the nature of these interfaces strongly affects sensor performance. In aluminium-contacted silicon nanowires, Schottky-type structures exhibit higher gas sensitivity than ohmic contacts [13], [14], [15] because the contact barrier amplifies responses to surface adsorption. Therefore, understanding and modelling contact electrostatics are not just a theoretical requirement but directly determine device optimisation.

Nevertheless, modelling this system presents a fundamental difficulty: in a doped semiconductor, the space charge near a contact originates from ionised dopants such that classical depletion electrostatics (space-charge region width and Schottky barrier height) are applied without difficulty. Meanwhile, in an undoped poly-SiNW, traps provide the fixed charge responsible for band bending, with their occupancy depending on the local potential and capture–emission mechanism [16]. Consequently, classical depletion models developed for doped junctions cannot be directly applied; thus, modelling most often relies on numerical simulations, whose accuracy comes at the cost of limited insight into underlying physical mechanisms and the scaling dependencies of the current.

The nature of a contact introduces a second complication: when a metal is deposited onto a disordered semiconductor, the high density of interface states pins the Fermi level, decoupling the barrier height from the metal and semiconductor work functions [17]. The effective barrier and hence band bending and the associated space charge cannot therefore be predicted using the Schottky–Mott rule; the barrier must instead be related to the density of states governing both interface pinning and bulk trapping [18].

In this context, we develop an analytical $I(V)$ model of a poly-SiNW Schottky-contacted resistor. We first establish the equilibrium potential by solving Poisson's equation, including the DOS-based trap densities. We then detail the FPR formation mechanisms by deriving analytical expressions for the free-hole concentration, electric field, and region width, which consequently afford $I(V)$ characteristic. These analytical expressions are validated by numerical simulations using Silvaco TCAD ATLAS [19].

2. Device Transport Modelling

2.1 Trap density model

Figure 1 displays a three-dimensional (3D) view of the modelled device and the corresponding equilibrium band diagram along the x-direction. Because the work function of aluminium ($\Phi_M \approx 4.1eV$) and electron affinity of silicon ($\chi \approx 4.17eV$) are nearly equal, the Schottky–Mott rule, $\Phi_b = \Phi_M - \chi$, will predict a negligible barrier height, incompatible with the observed band bending. The latter reflects the Fermi level pinned by the high density of states inherent to these nanowires, which fixes E_F near the midgap, independent of the work functions. The corresponding band diagram is shown in Figure 1: the Fermi level, pinned at the midgap near the contact, lies in the lower half of the bandgap deep into the nanowire, with band bending ψ_b corresponding to the bulk potential, whose origin and value are detailed in Section 2.2.

Previous studies [20] on the electrical properties of poly-SiNWs have revealed that the conduction mechanism operates via variable-range hopping (VRH), a characteristic of high density of electric traps afforded by the disordered structure of these nanowires.

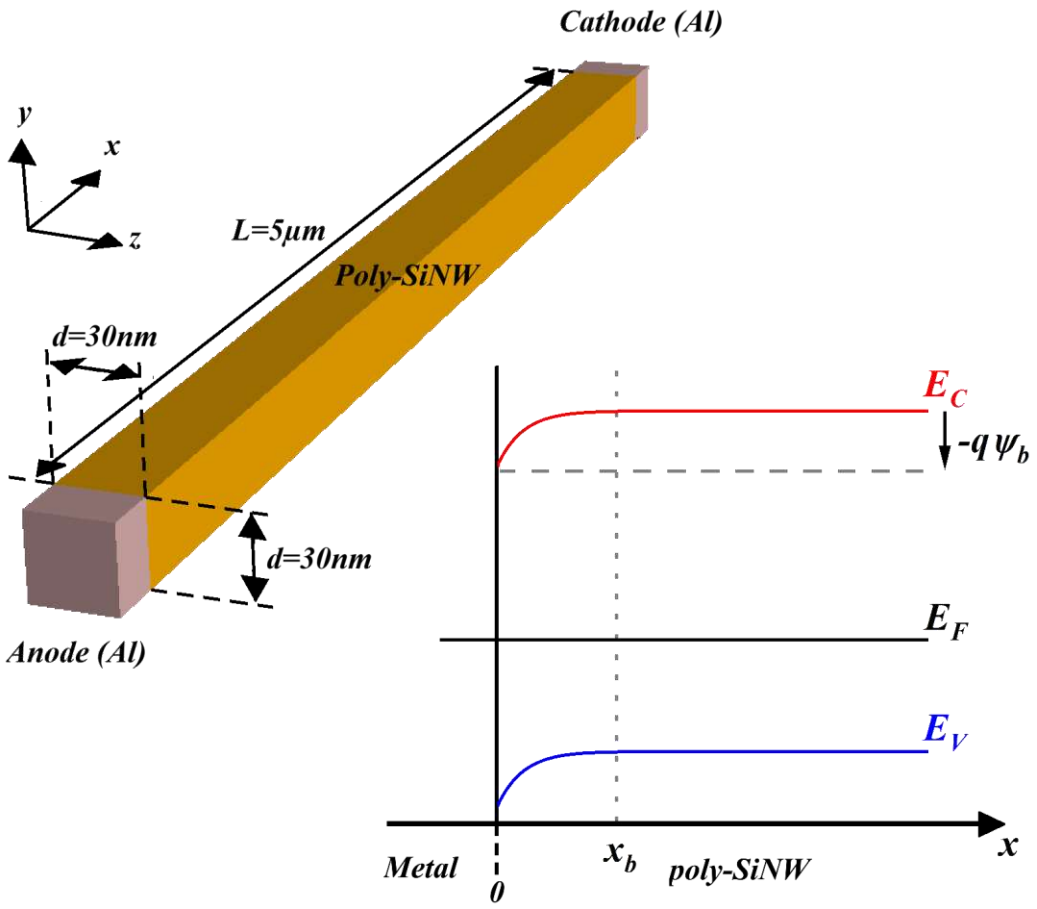

Fig. 1. 3D schematic of Al/poly-SiNW/Al resistor (not to scale) and equilibrium band diagram along the x-direction: bending of E_C and E_V over depths x_b and qψ_b places E_F in the lower half of the bandgap.

We therefore adopt the DOS model [16] to describe the distribution of these traps within the bandgap. The acceptor and donor trap densities are denoted by $g_A(E)$ and $g_D(E)$, respectively, each expressed as a double exponential for tail states and deep states; furthermore, their occupancy is governed by the occupation probability function $f(E)$.

$$g_{TA}(E) = N_{TA}\, exp\left(\frac{E - E_C}{w_{TA}}\right) \tag{1}$$

$$g_{DA}(E) = N_{DA}\, exp\left(\frac{E - E_C}{w_{DA}}\right) \tag{2}$$

$$g_{TD}(E) = N_{TD}\, exp\left(\frac{E_V - E}{w_{TD}}\right) \tag{3}$$

$$g_{DD}(E) = N_{DD}\, exp\left(\frac{E_V - E}{w_{DD}}\right) \tag{4}$$

Here, $g_{TA}(E)$ and $g_{TD}(E)$ are two exponential densities corresponding to the acceptor and donor trap densities of band tails, respectively. Similarly, $g_{DA}(E)$ and $g_{DD}(E)$ are two exponential densities corresponding to the acceptor and donor deep-state densities, respectively. E denotes the trap energy, E_C represents the conduction band energy, and E_V indicates the valence band energy. For tail distributions, the DOS is described by the densities of states at the conduction and valence band edges (N_{TA} and N_{TD}, respectively) and by the characteristic decay energies (W_{TA} and W_{TD}, respectively). For deep distributions, the DOS is described by the densities of states at the conduction and valence band edges (N_{DA} and N_{DD}, respectively) and by the characteristic decay energies (W_{DA} and W_{DD}, respectively). Table 1 lists the DOS parameters from Ref. [16].

The ionised trap densities for acceptor tails, acceptor deep levels, donor tails and donor deep levels, denoted as n_{tail}, n_{deep}, p_{tail} and p_{deep}, respectively, are calculated by integrating DOS distributions over the band gap.

$$n_{tail} = \int_{E_V}^{E_C} g_{TA}(E) f(E) dE \tag{5}$$

$$n_{deep} = \int_{E_V}^{E_C} g_{DA}(E) f(E) dE \tag{6}$$

$$p_{tail} = \int_{E_V}^{E_C} g_{TD}(E)(1 - f(E)) dE \tag{7}$$

$$p_{deep} = \int_{E_V}^{E_C} g_{DD}(E)(1 - f(E)) dE \tag{8}$$

where $f(E)$ is the trap occupation probability. Calculation of the ionised trap densities and expression of $f(E)$ are reported in the Appendix.

Table 1. Model parameters used in this study

Parameter	Value
N_{TA}	$10^{21} cm^{-3}.eV^{-1}$
N_{DA}	$2 \times 10^{20} cm^{-3}.eV^{-1}$
N_{TD}	$10^{21} cm^{-3}.eV^{-1}$
N_{DD}	$10^{18} cm^{-3}.eV^{-1}$
W_{TA}	$0.06\ eV$
W_{DA}	$0.1\ eV$
W_{TD}	$0.04\ eV$
W_{DD}	$0.1\ eV$
E_i	$0.56\ eV$
V_{th}	$0.0258\ V$
n_i	$6.67 \times 10^{9} cm^{-3}$

2.2 Equilibrium potential: trapped-charge screening

Figure 2 compares the ionised trap densities with TCAD simulations. A good agreement is observed over nearly two decades: the model captures both the order of magnitude and exponential dependence of trapped charges on the potential ψ, in particular, the opposite slopes of $\pm 1/W$ that distinguish acceptor traps from donor traps. This agreement, derived from purely analytical expressions, confirms the relevance of trapped-charge description governed by the density of states and validates the model established here.

The potential $\psi(x)$ along a nanowire is governed by one-dimensional Poisson's equation

$$\frac{\partial^2 \psi}{\partial x^2} = \frac{q}{\varepsilon_{si}} [N_t(x) - P_t(x) + n(x) - p(x)] \tag{9}$$

where $N_t(x) = n_{tail}(x) + n_{deep}(x)$ and $P_t(x) = p_{tail}(x) + p_{deep}(x)$ are the ionised trap densities and n and p are the free electron and hole concentrations, respectively. Free-carrier concentrations are given by the following Boltzmann relations:

$$n(x) = n_i exp\left(\frac{(\psi + \varphi_{fn})}{V_{th}}\right) \tag{10}$$

$$p(x) = n_i exp\left(-\frac{(\psi + \varphi_{fp})}{V_{th}}\right) \tag{11}$$

where φ_{fn} and φ_{fp} are the electron and hole quasi-Fermi levels, respectively, and V_{th} is the thermal voltage. At equilibrium, the electron and hole quasi-Fermi levels are flat and equal such that $\varphi_{fn}(x) = \varphi_{fp}(x) = 0V$, yielding the following equation:

$$\frac{\partial^2\psi(x)}{\partial x^2} = \frac{q}{\varepsilon_{si}}\left(g_{TA0}e^{\frac{q\psi}{w_{TA}}} + g_{DA0}e^{\frac{q\psi}{w_{DA}}} - g_{TD0}e^{-\frac{q\psi}{w_{TD}}} - g_{DD0}e^{-\frac{q\psi}{w_{DD}}}\right) \tag{12}$$

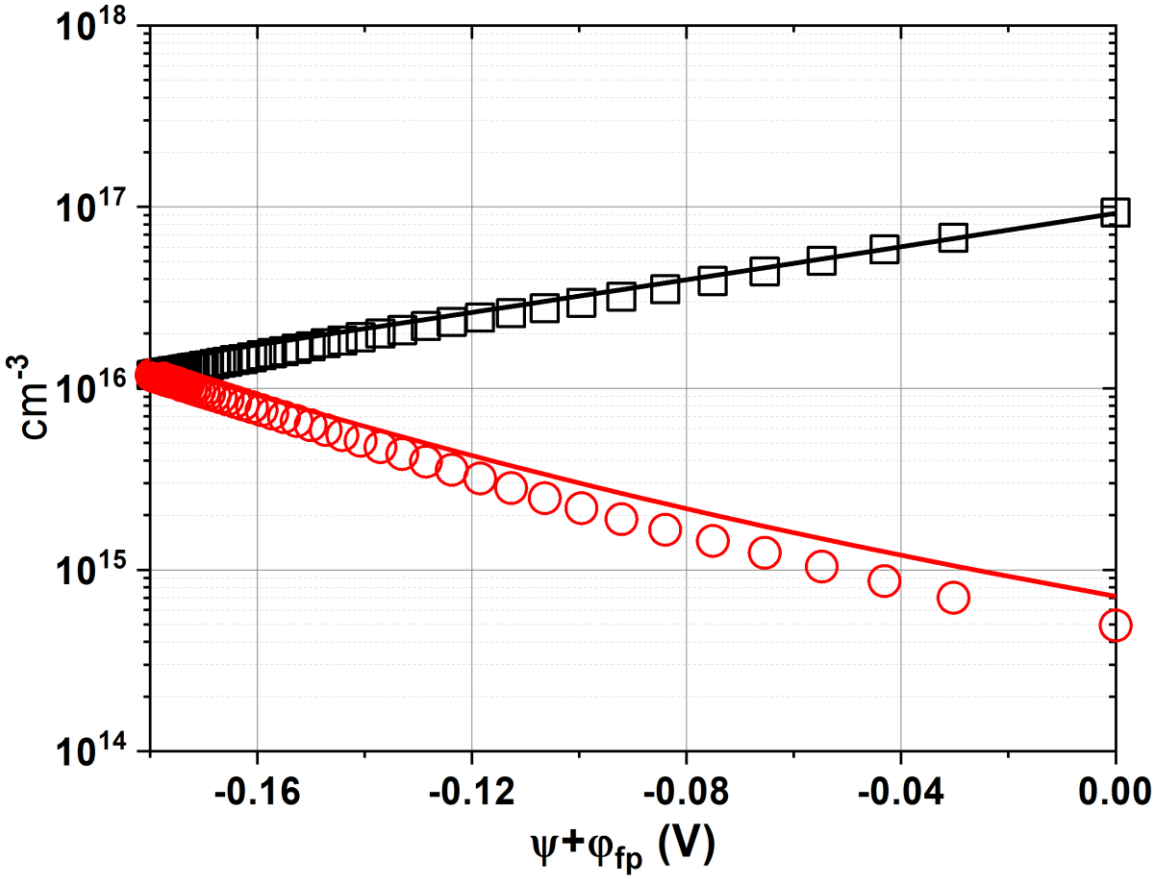

Fig. 2. Ionised trap densities $n_{Tail} + n_{deep}$ (black) and $p_{Tail} + p_{deep}$ (red) as a function of ψ. Symbols: TCAD simulation; lines: analytical model.

The free-carrier densities n and p are omitted from (5). Their scale is indeed determined by the intrinsic concentration n_i, which is five to seven orders of magnitude lower than the pre-factors g_0 ($10^{14} - 10^{17}\ cm^{-3}$) of trapped charges—a consequence of very high trap density of states ($N \sim 10^{21}\ cm^{-3}eV^{-1}$) inherent to disordered polycrystalline silicon. Moreover, as the characteristic decay w exceeds kT, trapped charges vary more slowly with ψ (as $e^{\pm\psi/w}$) than free carriers do (as $e^{\pm\psi/kT}$); the latter will become comparable only for $|\psi| \gtrsim 0.6$ V near band edges, lying outside the range considered here. The space charge is therefore entirely governed by traps.

Multiplying (12) by $2\,\partial\psi$ and integrating over ψ yield the following using the identity $d[(\partial\psi/\,\partial x)^2] = 2\,(\partial^2\psi/\,\partial x^2)\,d\psi$:

$$\xi(\psi)^2 = \frac{2q}{\varepsilon_{si}}\big(G_{Aw}(\psi) + G_{Dw}(\psi)\big) + C \tag{13}$$

where

$$G_{Aw}(\psi) = w_{TA}g_{TA0}e^{\frac{q\psi}{w_{TA}}} + w_{DA}g_{DA0}e^{\frac{q\psi}{w_{DA}}}$$

$$G_{Dw}(\psi) = w_{TD}g_{TD0}e^{-\frac{q\psi}{w_{TD}}} + w_{DD}g_{DD0}e^{-\frac{q\psi}{w_{DD}}}$$

where the integration constant C is fixed by the boundary condition: the field $\xi(\psi_b) \to 0$, i.e. requiring the field to vanish as the potential reaches its bulk value ψ_b, which yields the following equation:

$$\xi(\psi) = \sqrt{\frac{2q}{\varepsilon_{si}}\left[G_{Aw}(\psi - \psi_b) + G_{Dw}(\psi - \psi_b)\right]} \tag{14}$$

The neutrality condition deep within a nanowire, given by (15), is solved numerically and yields $\psi_b \approx -0.1786\,V$.

$$n_{tail}(\psi_b) + n_{deep}(\psi_b) - p_{tail}(\psi_b) - p_{deep}(\psi_b) = 0 \tag{15}$$

However, the potential cannot be analytically determined from (14). Nevertheless, Figure 3 reveals a remarkable trend in the plot of ξ against ψ: over the entire interval separating the bulk potential ψ_b from the contact ($\psi = 0$), the field is linear in ψ, which is exactly reproduced by the TCAD simulation. Therefore, one can write, over $[\psi_b, 0]$,

$$\xi(\psi) = \frac{\psi - \psi_b}{\lambda_0} = \frac{\psi}{\lambda_0} + \xi_0 \tag{16}$$

where the slope $\lambda_0 \approx 4.47 \times 10^{-6}\,cm$ and intercept $\xi_0 \approx 4 \times 10^4\,V.cm^{-1}$ are deduced from the characteristic (inset Figure 3).

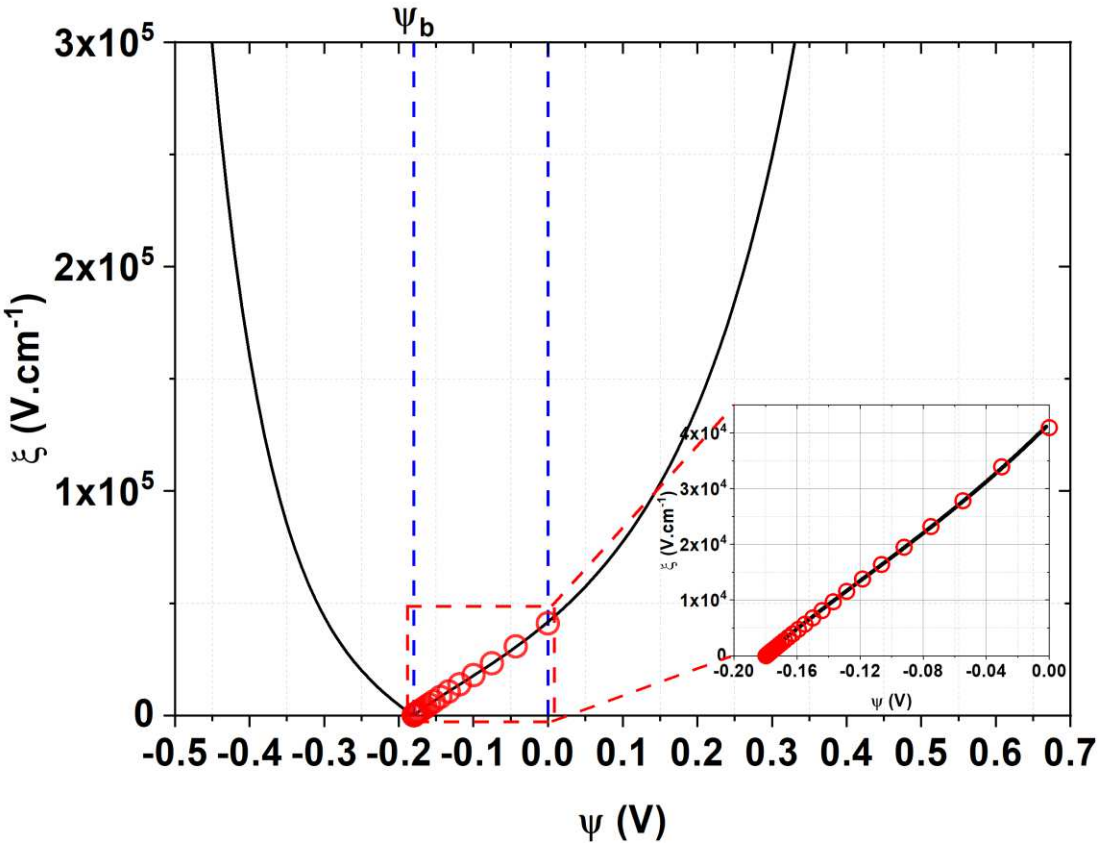

Fig. 3. Equilibrium electric field $\xi(\psi)$. Line: model; circles: TCAD simulation. ξ vanishes at the neutrality potential $\psi_b \simeq -0.1786\ V$. Inset: zoomed view of the interval $[\psi_b, 0]$, where ξ is linear in ψ.

This linearity permits analytical integration of the field–potential relation, directly yielding the profile $\psi(x)$. The field is derived from the potential as follows:

$$\xi(x) = -\frac{\partial \psi(x)}{\partial x} \tag{17}$$

Substituting the linear form $\xi = \psi/\lambda_0 + \xi_0$ and separating variables yield:

$$x = -\int \frac{d\psi}{\frac{\psi}{\lambda_0} + \xi_0} = -\lambda_0 ln\left(\frac{\psi}{\lambda_0} + \xi_0\right) + C \tag{18}$$

The constant C is determined by the interface condition, $\psi(0) = 0$, yielding $C = \lambda_0 ln(\xi_0)$. Noting that $\lambda_0 \xi_0 = -\psi_b$, we obtain $x = -\lambda_0 ln(1 - \psi/\psi_b)$; finally,

$$\psi(x) = \psi_b \left(1 - exp\left(-\frac{x}{\lambda_0}\right)\right) \tag{19}$$

Figure 4 compares the analytical profile $\psi(x) = \psi_b[1 - exp(-x/\lambda_0)]$ with the TCAD simulation, demonstrating excellent agreement. The potential decays from $\psi(0) = 0$ and

monotonically reaches the bulk potential $\psi_b \approx -0.1786\,V$. Relaxation is confined to first few tens of nanometres: the residual deviation from the bulk potential, $\psi_b - \psi(x) = \psi_b exp(-x/\lambda_0)$, becomes negligible beyond a depth denoted as $x_b \approx 0.31\,\mu m$, i.e. few screening lengths ($\lambda_0 \approx 44.7\,nm$).

This behaviour is the hallmark of electrostatic screening: potential perturbation imposed by the contact is neutralised over a characteristic length λ_0 via reorganisation of a trapped charge, which opposes it [21]. This mechanism is analogous to that of Debye screening for a trap-governed semiconductor [22]. The key distinction between trap-dominated screening and classical free-carrier screening lies in the origin of the response charge: the differential response of a trapped charge $|d\rho/d\psi|$, evaluated at the bulk state ψ_b is λ_0, the mobile carrier density.

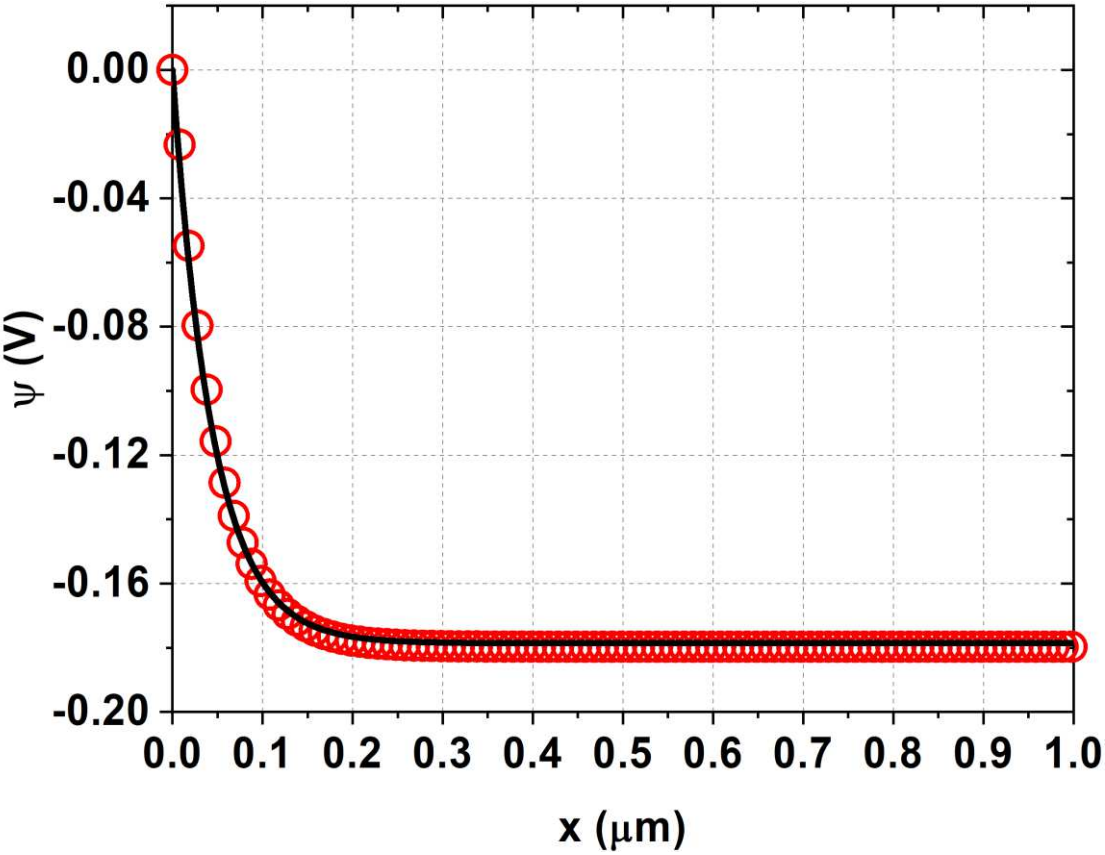

Fig. 4. Potential profile $\psi(x)$ at zero bias, from the contact ($x = 0$) into the bulk. Line: model, (19); symbols: TCAD simulation. Exponential relaxation from $\psi(0) = 0$ to $\psi_b \approx -0.1786\,V$ over $\lambda_0 \approx 44.7\,nm$.

2.3 Nonequilibrium: Fermi pinning region

Owing to the symmetry of the Al/poly-SiNW/Al structure, the sign of the applied bias V_A only reverses the current direction. Therefore, it is sufficient to consider the case $V_A > 0$. At the Al/poly-SiNW interface, the high density of acceptor and donor traps forces the Fermi level to be pinned at the midgap [23]. It follows that $\psi + \phi_{fp} = 0$ and $\psi + \phi_{fn} = 0$, leading to $p(x = 0) = n(x = 0) = n_i$. The charge density ρ_0 at the interface is entirely dominated by ionised traps such that $\rho_0 = \rho(0) \approx 6.5 \times 10^{16} cm^{-3}$

Thus, ρ_0 is a fixed space charge that, together with the applied bias, generates an electric field ξ' directed towards the depth of the nanowire. Intuitively, this field attracts electrons towards the contact, while holes are repelled towards the depth, thereby depleting the region near the contact of free carriers. One will then expect a classical depletion region to be created, where $n \ll n_i$ and $p \ll n_i$, extending over a width W. Beyond this region, equilibrium is restored with $p(x > W) = p(\psi_b)$ and $n(x > W) = n(\psi_b) \approx 6.4 \times 10^6 cm^{-3}$.

Moreover, ξ' decreases within this region, from its maximum value at the interface to the characteristic value ξ_0 of the equilibrium field at $x = W$. Consequently, Fermi-level pinning is no longer ensured at $x = W$, and the field ξ for $x > W$ attracts electrons from the depth towards the region near the contact, where the strong field ξ' accelerates them towards the contact. Conversely, the hole concentration in the region near the contact exhibits a typical evolution, resulting from two mechanisms: Fermi-level pinning at the interface and the spatial decay of the electric field ξ'. Indeed, hole transport in this region is pure drift current [24], whose density J_p is expressed as follows:

$$J_p(x) = q\mu_p p(x)\xi'(x) \tag{20}$$

where μ_p denotes hole mobility. In the steady state, charge conservation imposes the following continuity equation:

$$\frac{dJ_p}{dx} = -qR_{n,p} \tag{21}$$

where $R_{n,p}$ denotes the generation/recombination rate, defined according to the Shockley–Read–Hall (SRH) model for traps [25], as follows:

$$R_{n,p} = \sum_i \int_{E_V}^{E_C} h_i(E) g_i(E) dE \tag{22}$$

where $g_i(E)$ denotes the density of states of each trap family ($n_{tail}(E)$, $n_{deep}(E)$, $p_{tail}(E)$, and $p_{deep}(E)$) and $h_i(E)$ is the SRH kernel, whose explicit expression is given in Appendix. Calculation of $R_{n,p}$ is not detailed here; we will merely evaluate it numerically for $n \ll n_i$ and $p \in [p,(0) = n_i p(x \gg W) = p(\psi_b) \approx 10^3 n_i]$. This yields a negative $R_{n,p}$ value, varying in the range $[-2.35 \times 10^{19}\ cm^{-3}.s^{-1}, -4.8 \times 10^{17} cm^{-3}.s^{-1}]$. Consequently, dJ_p/dx lies in the range $[7.68 \times 10^{-2}\ A.cm^{-3}, 3.76 \times A.cm^{-3}]$. The variation in J_p is only noticeable for very large widths W (on the order of few micrometres). For example, for $W = 1\ \mu m$, $\Delta J_p = \left(dJ_p/dx\right) \times W$ remains in the range $[7.68 \times 10^{-6} A.cm^{-2}, 3.76 \times 10^{-4} A.cm^{-2}]$. Even for a field $\xi'(0)$ slightly larger than ξ_0—taking $\Delta J_p = 3.76 \times 10^{-4}\ A.cm^{-2}$ and $J_p(0) = q\mu_p n_i \xi_0 \approx 2.1 \times 10^{-2}\ A.cm^{-2}$—$J_p(W) = J_p(0) + \Delta J_p \approx J_p(0)$.

Thus, we can consider J_p to be quasi-constant in this region for any $V_A > 0$. The free-hole concentration can then be deduced as follows:

$$p(x) = \frac{J_p(x)}{q\mu_p \xi'(x)} = \frac{J_p(0)}{q\mu_p \xi'(x)} = n_i \frac{\xi'_s}{\xi'(x)} \tag{23}$$

where $\xi'_s = \xi'(0)$. From (11), we can deduce expression for $\psi + \phi_{fp}$ as follows:

$$\psi(x) + \varphi_{fp}(x) = -V_{th} \times ln\left(\frac{\xi'_s}{\xi'(x)}\right) \tag{24}$$

For $x = W$, $\psi(W) + \phi_{fp}(W) = -V_{th} \times ln(\xi'_s/\xi_0)$. As an example, simulation shows that $\xi'_s \sim 4.2 \times 10^5 V.cm^{-1}$ at $V_A = 10V$, a value close to the maximum value reported in **[26]**, yielding $\psi(W) + \phi_{fp}(W) \sim -59\ mV$. Over this region, the hole concentration varies from $p(0) = n_i$ to $p(W) \simeq 10 n_i$, corresponding to a relative increase of $\Delta p/p(0) \simeq 9$. Although this variation is not negligible in relative terms, the absolute change $\Delta p \sim 9 \times 10^{10} cm^{-3}$ remains far below the ionised trap density ($\sim 10^{16} - 10^{17} cm^{-3}$), thereby having a negligible effect on the space-charge density. This is confirmed by numerical evaluation, which yields $\Delta\rho/\rho_0 = [\rho_0 - \rho(W)]/\rho_0 \sim 10\%$, signifying a quasi-constant space charge. Consequently, we can consider ρ to be quasi-constant in this region and equal to ρ_0.

Thus, the aforementioned mechanisms characterise a region whose behaviour is neither that of a classical depletion region nor that of a neutral material. This region derives its specificity from pinning of the hole quasi-Fermi level to the intrinsic level, which maintains $p(x)$ on the order of few n_i. We therefore propose to designate this region as the Fermi pinning region (FPR) to

emphasise its physical origin and to distinguish it from conventional space-charge region models. Substituting ρ_0 into Poisson's equation and integrating over x yield an expression of the electric field

$$\xi'(x) = \xi'_s - q\frac{\rho_0}{\varepsilon_{si}}x \tag{25}$$

With $\xi'(W) = \xi_0$, the FPR width is given by

$$W = \frac{\varepsilon_{si}}{q\rho_0}(\xi'_s - \xi_0) \tag{26}$$

(26) correlates the width to the interface field, but ξ'_s remains undetermined as a function of V_A. Figure 5 plots ${\xi'_s}^2 - \xi_0^2$ versus V_A, observing a linear relationship that yields the following:

$${\xi'_s}^2 - \xi_0^2 = \sigma V_A \tag{27}$$

where σ is the slope of the linear fit in Figure 5. This is the typical form expected for the depletion electrostatics of a Schottky contact [27], i.e. $2q\rho_0/\varepsilon_{si}$, where ρ_0 is the fixed charge density. The analogy is not complete*;* however*,* in a conventional Schottky contact, this charge originates from ionised dopants, while here*,* it originates from the trapped charge frozen under bias. Equating the measured slope to $\sigma = 2q\rho_0/\varepsilon_{si}$ yields $\rho_0 = \sigma\varepsilon_{si}/2q \approx 5.75 \times 10^{16}\ cm^{-3}$. This value agrees well with the net charge derived from the trap density of states; this consistency confirms the interpretation of the slope.

Substituting (27) into (26) yields

$$W = \frac{\varepsilon_{si}}{q\rho_0}\left(\sqrt{\sigma V_A + \xi_0^2} - \xi_0\right) \tag{28}$$

These expressions warrant two remarks. First, for $V_A = 0$, $\xi'_s = \xi_0$ and $W = 0$*,* we continuously recover the equilibrium situation, with ξ_0 acting as a screening field at the contact. Second, for $V_A > 0$, ξ_0 reflects the pre-existing equilibrium field and rounds off this dependence. This corresponds to the FPR, inserted by the bias ahead of the equilibrium screening region: the applied bias pushes this region deeper into the nanowire over a depth $W \propto \sqrt{V_A}$, without significantly altering trap occupancy beyond $x = W$, wherein the potential profile remains as established at equilibrium.

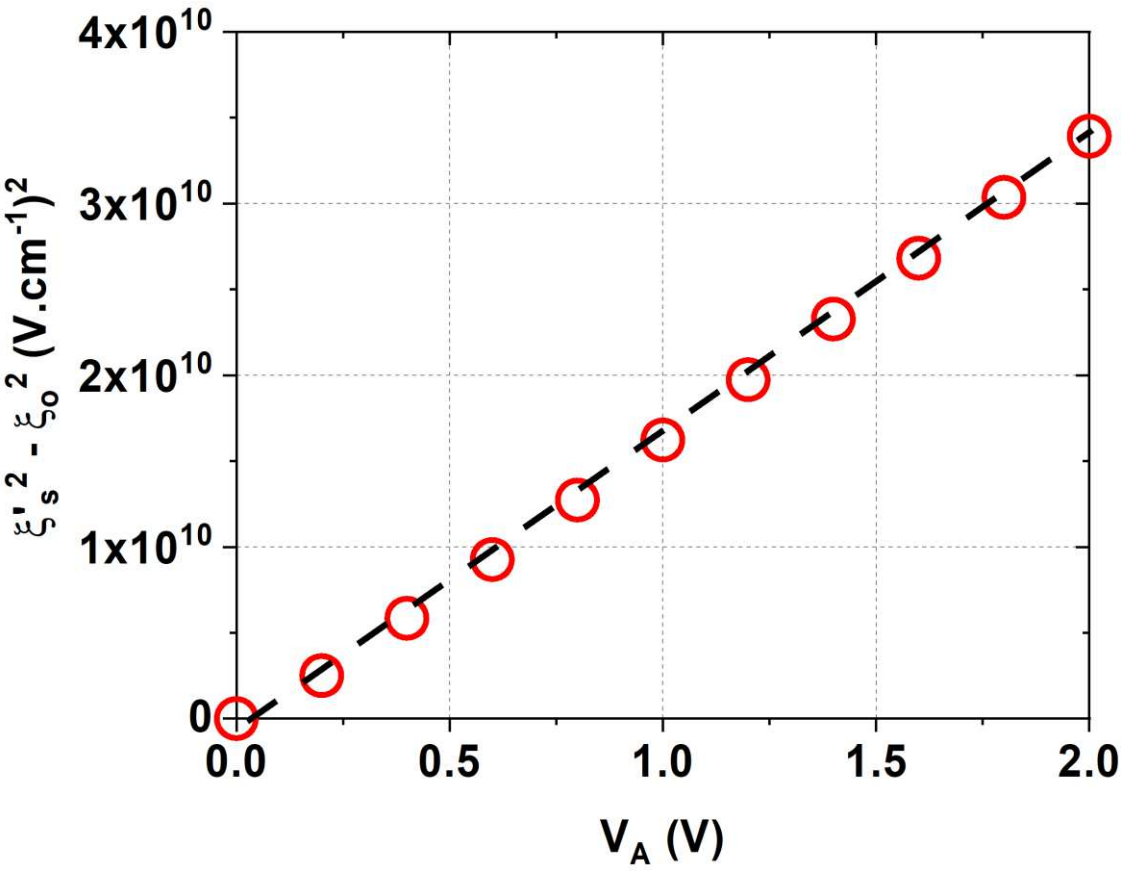

Fig. 5. $\xi_s'^{\,2} - \xi_0^2$ as a function of V_A, derived from the simulated field profiles. The origin–intercept linear fit $\xi_s'^{\,2} - \xi_0^2 = \sigma V_A$ with $\sigma \approx 1.77 \times 10^{10}\ V.cm^{-2}$.

2.4 I(V) Characteristic

The hole current in the nanowire is expressed compactly within the drift–diffusion formalism via the gradient of the hole quasi-Fermi potential

$$J_P = -q\mu_p p \frac{d\varphi_p}{dx} \tag{29}$$

This formulation combines the drift and diffusion contributions into a single term. In the steady state, J_p is uniform along the nanowire and can therefore be evaluated in the deep bulk, where the free-hole density reaches its maximum $p(\psi_b)$—i.e., the equilibrium value—and ϕ_{fp} varies smoothly. In this region, $\psi + \phi_{fp} = \psi_b$ is constant, yielding $d(\psi + \phi_{fp})/dx = 0$ and

$$\frac{d\varphi_p}{dx} = -\frac{d\psi}{dx} \tag{30}$$

Although $\psi + \phi_{fp}$ is rigorously flat, ψ and ϕ_{fp} retain opposite and non-zero gradients. Beyond the FPR, trap occupancy ceases to freeze, and equilibrium is restored. Following the profile established in (19), $\psi + \phi_{fp}$ can be expressed as a shift W such that

$$\psi(x) + \phi_{fp}(x) = \psi_b \left(1 - exp\left(-\frac{(x - W)}{\lambda_0}\right)\right) \tag{31}$$

The associated charge density is as follows:

$$\rho(x) = \rho_0 exp\left(-\frac{(x - W)}{\lambda_0}\right) \tag{32}$$

Inserting Poisson's equation, $d\xi/dx = -\rho(x)/\varepsilon_{si}$, with the charge density (32) yielding the following field:

$$\xi(x) = \frac{\rho_0 \lambda_0}{\varepsilon_{si}} exp\left(-\frac{(x - W)}{\lambda_0}\right) + C \tag{33}$$

In the deep bulk, the exponential term vanishes, and the integration constant must equal the equilibrium field denoted as ξ_b. Thus, $C = \xi_b$. Applying this to (33) and using the boundary condition at $x = W$, where the field reaches the typical value ξ_0, yield the following compact profile:

$$\xi(x) = \xi_b + (\xi_0 - \xi_b) exp\left(-\frac{(x - W)}{\lambda_0}\right) \tag{34}$$

Figure 6 shows the simulated field profiles on a logarithmic scale for V_A from 0 to 2 V in 0.4 V steps. At equilibrium, the field decays exponentially from ξ_0 and vanishes beyond x_b. Under bias, each profile decays with the same slope, confirming the invariance of λ_0; however, they plateau at ξ_b in the deep bulk, whose height increases with increasing voltage.

These profiles are self-similar, as directly visible in the figure: on a logarithmic scale, increasing voltage shifts the entire profile upwards, while the curves remain parallel in the decay region. The screening tail, governed by λ_0—which depends only on ψ_b and remains unchanged under bias—maintains the shape, varying only the amplitude.

Because the deep field vanishes at equilibrium, where ξ'_s reduces to ξ_0, not the entire interface field, only the excess induced by the bias is transmitted into the bulk to set ξ_b. The inset of Figure 6 quantifies this, plotting ξ_b versus ξ'_s. The curve starts from $\xi'_s = \xi_0$ at $\xi_b = 0$, confirming that the bulk field vanishes at equilibrium; furthermore, the curve then grows hyperbolically. This behaviour reflects a quadrature dependence between the two fields

$$\xi_b = k\sqrt{\xi_s'^2 - \xi_0^2} \tag{35}$$

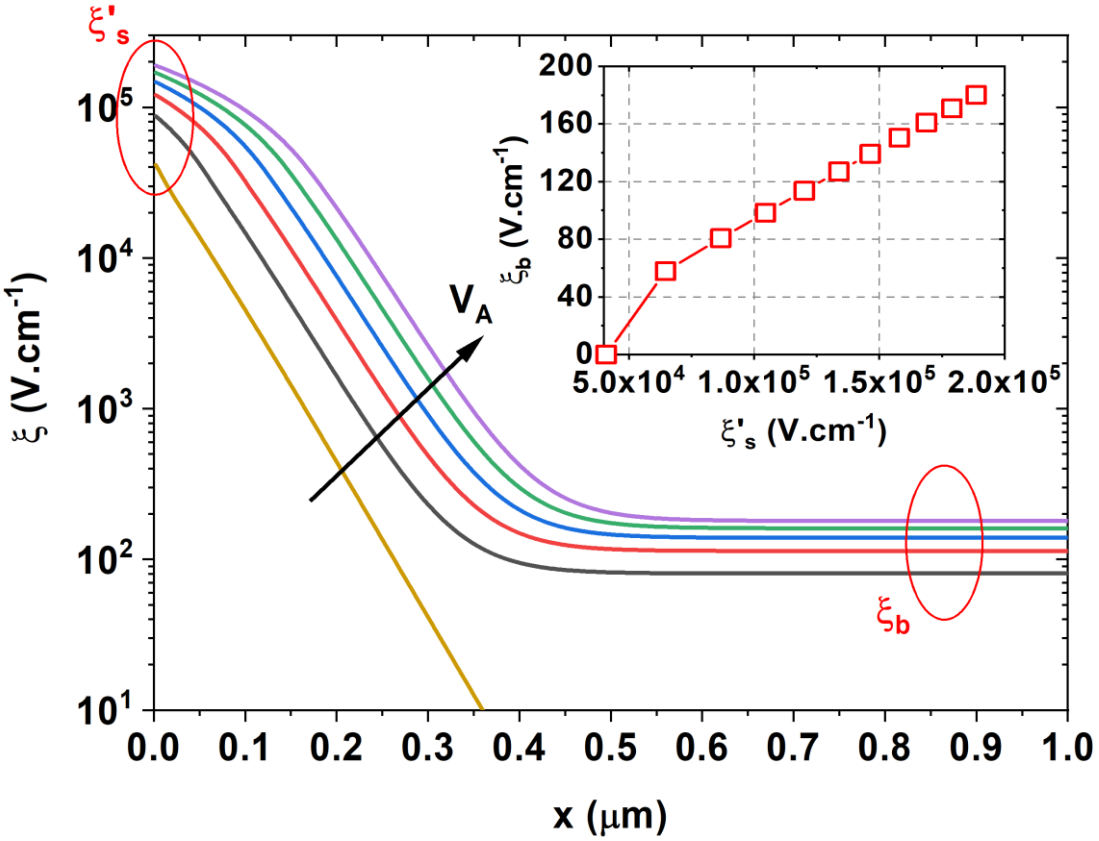

Fig. 6. Logarithmic field profiles $\xi(x)$ for V_A from 0 to 2 V ($0.4\,V$ steps). Field decays from ξ'_s over λ_0 and plateaus at ξ_b. Inset: ξ_b versus ξ'_s.

Figure 7 plots ξ_b versus $\left(\xi_s'^2 - \xi_0^2\right)^{1/2}$. The plot is linear and crosses the origin; the slope yields the proportionality factor k. This ensures that the background field vanishes at equilibrium ($\xi_s' = \xi_0$). In the deep bulk, the screening tail originating from the interface field reaches ξ_b. Evaluating (10) at x_b, wherein the equilibrium potential relaxes to ψ_b (Figure 4), gives the exponential factor $exp(-x_b/\lambda_0)$; the tail is attenuated by this factor. We therefore set

$$k = exp\left(-\frac{x_b}{\lambda_0}\right) \tag{36}$$

The same distance x_b governs both potential relaxation at equilibrium and field attenuation under bias—which is no coincidence: both are manifestations of the same screening decay over λ_0. The value $k \approx 9.33 \times 10^{-4}$, derived from the slope of Figure 7, corresponds to $x_b \approx 0.32\mu m$, in agreement with the potential relaxation observed in Figure 4. The inset illustrates this attenuation on a characteristic field profile.

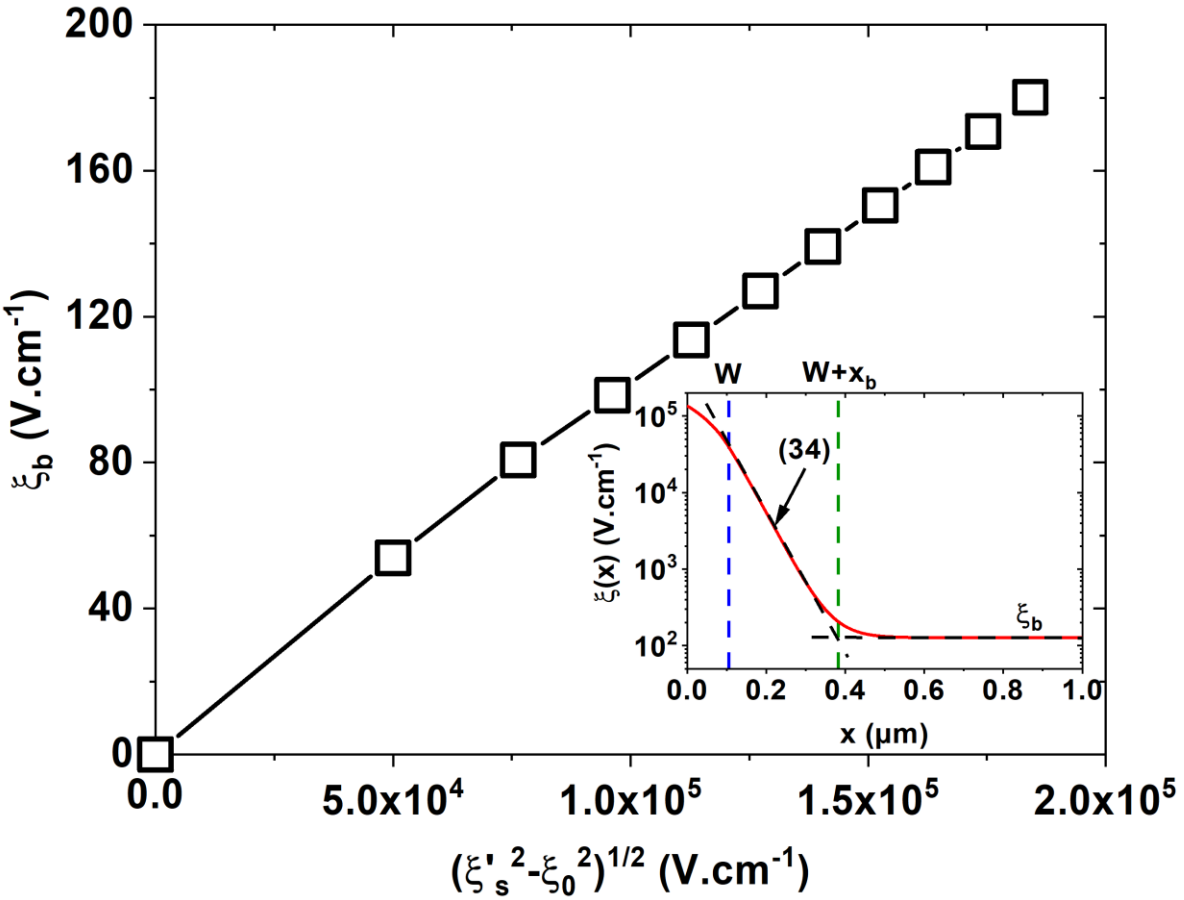

Fig. 7 ξ_b versus $\left(\xi_s'^{\,2} - \xi_0^2\right)^{1/2}$: origin–intercept line with slope $k = exp(-x_b/\lambda_0)$. Inset: semi-log $\xi(x)$ profile decaying as $exp(-x/\lambda_0)$ for $x > W$ towards ξ_b, intersecting at $x = W + x_b$.

As stated above, J_p is evaluated in the deep bulk of the nanowire, where $p(\psi_b)$ is maximum. From the current density (29), we obtain the following:

$$J_p = q\mu_p p(\psi_b)\xi_b \tag{37}$$

Combining (27), (35) and (36) with the current density (37) and multiplying by the cross-sectional area S yield the total current

$$I = q\mu_p p(\psi_b) exp(-x_b/\lambda_0) S\sqrt{\sigma V_A} \tag{38}$$

Figure 8 confirms the proportionality $I \propto \sqrt{V_A}$ from the $I(V_A)$ characteristic. This square-root dependence captures the underlying mechanism: the applied bias sets the interface field via depletion electrostatics, $\xi'_s \propto \sqrt{V_A}$. This field extends deep into the nanowire along the depletion region and screening tail, attenuated by $exp(-x_b/\lambda_0)$, establishing the background field ξ_b in the bulk, which drives holes through the quasi-neutral region and sets the current.

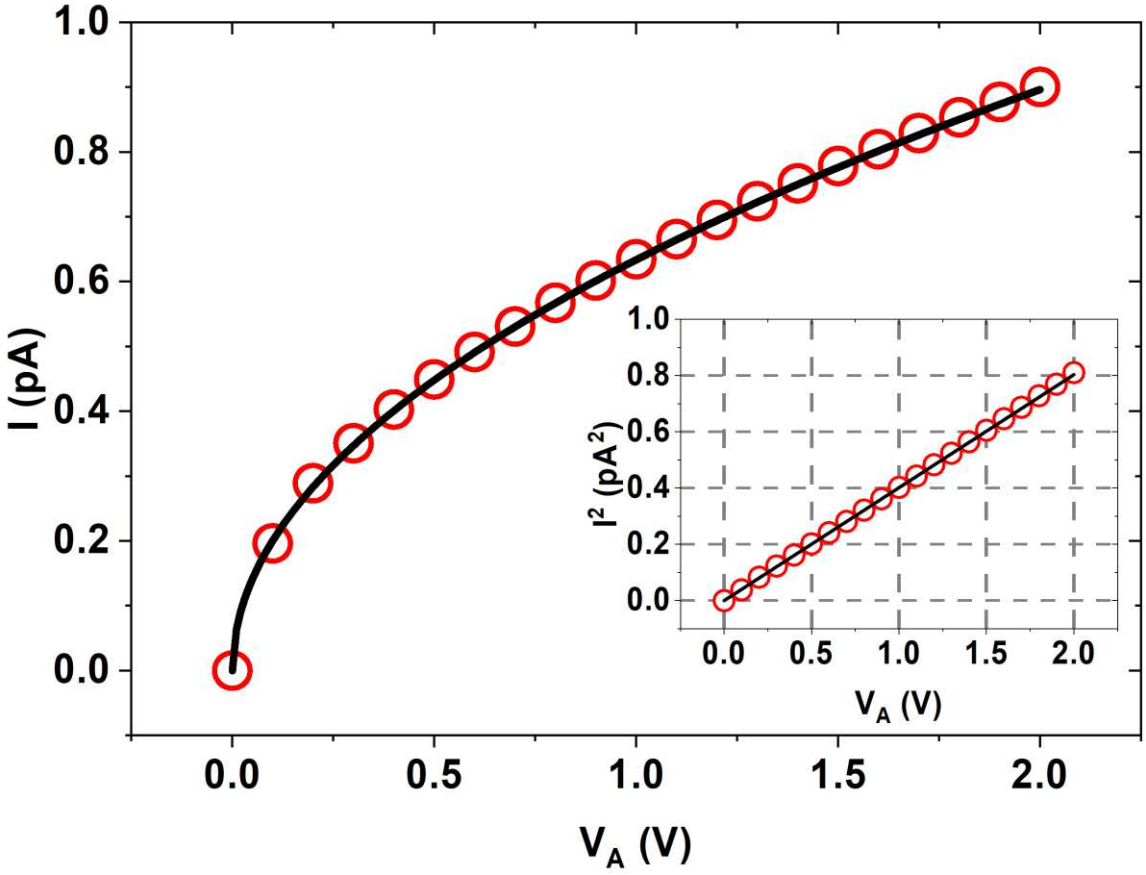

Fig. 8 $I(V_A)$ characteristic: TCAD simulation (circles) and analytical model (38) (line). Inset: I^2 versus V_A; the linear dependence through the origin confirms$I \propto \sqrt{V_A}$

3. Conclusion

We develop an analytical model for the $I(V)$ characteristic of an undoped poly-SiNW Schottky-contacted resistor. At equilibrium, the contact induces a perturbation, which—through an electrostatic screening effect—defines the profiles of trapped charges and free carriers. This phenomenon manifests as an equilibrium field at the interface and as a potential that relaxes exponentially over a characteristic length down to a negative bulk value, dependent on the DOS parameters.

Out of equilibrium, a typical region forms near the metal/poly-SiNW interface. Unlike a classical depletion region, this region—which we refer to as the Fermi pinning region—is characterised by frozen trap occupancy and a free-hole concentration of the order of few n_i. Beyond the FPR, equilibrium is restored, and a residual field—an attenuated replica of the interface field transmitted through the FPR and screening regions—ensures the drift of free holes in the bulk. The

$\sqrt{V}$ dependence of this field ultimately yields an $I(V)$ characteristic of the form $I \propto \sqrt{V}$. The formulations established and discussed in this study are validated by numerical simulations performed using Silvaco TCAD ATLAS, showing excellent quantitative agreement.

In contrast to empirical descriptions of $I(V)$ characteristic, this study proposes an original analytical framework that elucidates microscopic mechanisms governing transport in undoped poly-SiNW Schottky-contacted resistors. By establishing a direct link among Schottky contact electrostatics, the trap density of states, and the current–voltage response, the model provides a comprehensive interpretation of device operation. This foundation opens a route for analytical modelling of Schottky-contact sensors, which exhibit high sensitivity compared with their ohmic counterparts.

4. Appendix

4.1 Probability occupation function $f(E)$

The trap occupation probability $f(E)$ follows the Shockley–Read–Hall (SRH) statistics **[25]**

$$f(E) = \frac{C_n n + C_p n_i exp\left(\frac{E_i - E}{kT}\right)}{C_n\left[n + n_i exp\left(\frac{E - E_i}{kT}\right)\right] + C_p\left[p + n_i exp\left(\frac{E_i - E}{kT}\right)\right]}$$

where $C_n = v_n \sigma_n$ and $C_p = v_p \sigma_p$ are the electron and hole capture probabilities per unit time, respectively. (v_n and v_p are the thermal velocities, and σ_n and σ_p are the capture cross-sections), E_i is the intrinsic energy level. At equilibrium, the above expression reduces to the following Fermi–Dirac distribution [16]:

$$f(E) = \frac{1}{1 + exp\left(\frac{E - E_F}{kT}\right)}$$

4.2 Equilibrium acceptor trap density

Given the similarity in form between expressions for $g_{TA}(E)$ and $g_{DA}(E)$, we detail here only calculation for n_{Tail}; n_{deep} is obtained by simply substituting the parameters (N_{DA}, w_{DA}). $f(E)$ can be approximated by intervals such that

For $E < E_F$, $f(E) \simeq 1$, and for $E > E_F$, $f(E) \simeq exp(E_F - E/kT)$. Thus,

$$n_{tail} = N_{TA}\int_{E_V}^{E_F} exp\left(\frac{E - E_C}{w_{TA}}\right) dE + N_{TA}\int_{E_F}^{E_C} exp\left(\frac{E - E_C}{w_{TA}}\right) exp\left(\frac{E_F - E}{kT}\right) dE$$

At equilibrium, $E_F = E_i + q\psi$. Introducing pre-factors g_{TA0} and g_{DA0}

$$n_{tail} = g_{TA0} exp\left(\frac{q\psi}{w_{TA}}\right), n_{deep} = g_{DA0} exp\left(\frac{q\psi}{w_{DA}}\right)$$

With

$$g_{TA0} = \frac{w_{TA}^2 N_{TA}}{w_{TA} - kT} exp\left(-\frac{E_i}{w_{TA}}\right), g_{DA0} = \frac{w_{DA}^2 N_{DA}}{w_{DA} - kT} exp\left(-\frac{E_i}{w_{DA}}\right)$$

4.3 Equilibrium donor trap density

Here, we detail calculation for p_{tail}; p_{deep} is deduced by substituting the parameters (N_{DD}, w_{DD}). Similarly, $1 - f(E)$ can be approximated by intervals such that for $E < E_F$, $1 - f(E) \simeq exp\left(\frac{E-E_F}{kT}\right)$, and for $E > E_F$,$1 - f(E) \simeq 1$. Thus,

$$p_{tail} = N_{TD} \int_{E_V}^{E_F} exp\left(\frac{E_V - E}{w_{TD}}\right) exp\left(\frac{E - E_F}{kT}\right) dE + N_{TD} \int_{E_F}^{E_C} exp\left(\frac{E_V - E}{w_{TD}}\right) dE$$

Introducing pre-factors g_{TD0} and g_{DD0}

$$p_{tail} = g_{TD0} exp\left(-\frac{q\psi}{w_{TD}}\right), p_{deep} = g_{DD0} exp\left(-\frac{q\psi}{w_{DD}}\right)$$

With

$$g_{TD0} = \frac{w_{TD}^2 N_{TD}}{w_{TD} - kT} exp\left(-\frac{E_i}{w_{TD}}\right), g_{DD0} = \frac{w_{DD}^2 N_{DD}}{w_{DD} - kT} exp\left(-\frac{E_i}{w_{DD}}\right)$$

4.4 SRH Kernel $h_i(E)$ function

The SRH kernel $h_i(E)$ used in Eq. (23) in the main text is defined as follows:

$$h_i(E) = \frac{v_n v_p \sigma_{iE} \sigma_{iH} (np - n_i^2)}{v_n \sigma_{iE} \left(n + n_i e^{\left(\frac{E-E_i}{kT}\right)}\right) + v_p \sigma_{iH} \left(p + n_i e^{\left(\frac{E_i-E}{kT}\right)}\right)}$$

where σ_{iE} and σ_{iH} are the electron and hole capture cross-sections for the i-th trap family, respectively.

References

[1] Demami, F., Rogel, R., Salaün, A. C., & Pichon, L. (2011). Electrical properties of polysilicon nanowires for device applications. *physica status solidi c*, 8 (3), 827-830. https://doi.org/10.1002/pssc.201000227

[2] Schmidt, V., Wittemann, J. V., & Gosele, U. (2010). Growth, thermodynamics, and electrical properties of silicon nanowires. *Chemical reviews*, 110 (1), 361-388. https://doi.org/10.1021/cr900141g

[3] Su, C. J., Tsai, T. I., Liou, Y. L., Lin, Z. M., Lin, H. C., & Chao, T. S. (2011). Gate-all-around junctionless transistors with heavily doped polysilicon nanowire channels. *IEEE Electron Device Letters*, 32 (4), 521-523. https://doi.org/10.1109/LED.2011.2107498

[4] Jamaa, M. H. B., Cerofolini, G., De Micheli, G., & Leblebici, Y. (2010). Polysilicon nanowire transistors and arrays fabricated with the multispacer technique. *IEEE transactions on nanotechnology*, 10 (4), 891-899. https://doi.org/10.1109/TNANO.2010.2089532

[5] Ouerghi, I., Philippe, J., Duraffourg, L., Laurent, L., Testini, A., Benedetto, K., ... & Ernst, T. (2014, December). High performance polysilicon nanowire NEMS for CMOS embedded nanosensors. In *2014 IEEE international electron devices meeting* (pp. 22-4). IEEE. https://doi.org/10.1109/IEDM.2014.7047101

[6] Maflin Shaby, S., & Vimala Juliet, A. (2012). Analysis and optimization of sensitivity of a MEMS peizoresistive pressure sensor. *Advanced Materials Research*, *548*, 652-656. https://doi.org/10.4028/www.scientific.net/AMR.548.652

[7] Demami, F., Ni, L., Rogel, R., Salaun, A. C., & Pichon, L. (2012). Silicon nanowires based resistors as gas sensors. *Sensors and Actuators B: Chemical*, *170*, 158-162. https://doi.org/10.1016/j.snb.2011.04.083

[8] Wenga, G., Jacques, E., Salaün, A. C., Rogel, R., Pichon, L., & Geneste, F. (2013). Step-gate polysilicon nanowires field effect transistor compatible with CMOS technology for label-free DNA biosensor. *Biosensors and Bioelectronics*, 40 (1), 141-146. https://doi.org/10.1016/j.bios.2012.07.001

[9] J. Kim, H. Oh, J. Lee, C.-K. Baek, M. Meyyappan, J.-S. Lee, « Three-dimensional simulation of threshold voltage variations due to an oblique single grain boundary in sub-40 nm polysilicon nanowire FETs », Semicond. Sci. Technol. 30, 085015 (2015). https://doi.org/10.1088/0268-1242/30/8/085015

[10] H. Oh, J. Kim, J. Lee, T. Rim, C.-K. Baek, J.-S. Lee, « Effects of single grain boundary and random interface traps on electrical variations of sub-30 nm polysilicon nanowire structures », Microelectron. Eng. 149, 113–117 (2016). https://doi.org/10.1016/j.mee.2015.09.018

[11] Siddique, A. B., Rahman, K. A., Alam, M. N., Hasan, K., & Hakim, M. M. A. (2018, December). Physical understanding on the interface states and grain boundary defects of polysilicon nanowires. In *2018 10th International Conference on Electrical and Computer Engineering (ICECE)* (pp. 213-216). IEEE. https://doi.org/10.1109/ICECE.2018.8636707

[12] Le Borgne, B., Pichon, L., Salaun, A. C., Le Bihan, B., Jolivet-Gougeon, A., Martin, S., Rogel, R., & de Sagazan, O. (2018).Bacteria electrical detection using 3D silicon nanowires based resistor. *Sensors and Actuators B: Chemical*, 273, 1794-1799. https://doi.org/10.1016/j.snb.2018.07.101

[13] Kondratev, V. M., Vyacheslavova, E. A., Shugabaev, T., Kirilenko, D. A., Kuznetsov, A., Kadinskaya, S. A., Shomakhov, Z. V., Baranov, A. I., Nalimova, S. S., Moshnikov, V. A., Gudovskikh, A. S., & Bolshakov, A. D. (2023). Si nanowire-based Schottky sensors for selective sensing of NH_3 and HCl via impedance spectroscopy. *ACS Applied Nano Materials*, 6(13), 11513-11523. https://doi.org/10.1021/acsanm.3c01545

[14] Meng, J., & Li, Z. (2020). Schottky-contacted nanowire sensors. *Advanced Materials*, *32*(28), 2000130. https://doi.org/10.1002/adma.202000130

[15] Pristavu, G., Pascu, R., Popescu, M., Simion, M., Romanitan, C., Mihalache, I., ... & Brezeanu, G. (2026). Silicon Nanowire-Based Schottky Diodes for Enhanced Temperature Sensing and Extended Operable Range. *Sensors*, *26*(3), 780. https://doi.org/10.3390/s26030780

[16] Demami, F. (2023). Polycrystalline silicon nanowire FET performance depending on density of states. *Journal of Computational Electronics*, *22*(4), 946-953. https://doi.org/10.1007/s10825-023-02034-8

[17] Newman, N., Spicer, W. E., Kendelewicz, T., & Lindau, I. (1986). On the Fermi level pinning behavior of metal/III–V semiconductor interfaces. *Journal of Vacuum Science & Technology B: Microelectronics Processing and Phenomena*, *4*(4), 931-938. https://doi.org/10.1116/1.583494

[18] Tung, R. T. (2014). The physics and chemistry of the Schottky barrier height. *Applied Physics Reviews*, *1*(1). https://doi.org/10.1063/1.4858400

[19] ATLAS User's Manual, Silvaco Software. 5.19.20.R (2013)

[20] Pichon, L., Jacques, E., Rogel, R., Salaun, A. C., & Demami, F. (2013). Variable range hopping conduction in N-and P-type in situ doped polycrystalline silicon nanowires. *Semiconductor science and technology*, *28*(2), 025002. https://doi.org/10.1088/0268-1242/28/2/025002

[21] Hung, Y. J., Lee, S. L., Beng, L. C., Chang, H. C., Huang, Y. J., Lee, K. Y., & Huang, Y. S. (2014). Relaxing the electrostatic screening effect by patterning vertically-aligned silicon nanowire arrays into bundles for field emission application. *Thin Solid Films*, *556*, 146-154. https://doi.org/10.1016/j.tsf.2014.01.040

[22] Brydges, D. C., & Federbush, P. (1981). Debye screening in classical Coulomb systems. In *Rigorous Atomic and Molecular Physics* (pp. 371-439). Boston, MA: Springer US. https://doi.org/10.1007/978-1-4613-3350-0_9

[23] Shao, G. (2021), Work Function and Electron Affinity of Semiconductors: Doping Effect and Complication due to Fermi Level Pinning. Energy Environ. Mater., 4: 273-276. https://doi.org/10.1002/eem2.12218

[24] Mak, D. K. (2003). Carrier Concentrations and Drift Currents in the Depletion Region of ap–n Junction. Surface Review and Letters, 10(04), 649-660. https://doi.org/10.1142/S0218625X03005360

[25] Shockley, W. T. R. W., & Read Jr, W. T. (1952). Statistics of the recombinations of holes and electrons. Physical review, 87(5), 835. https://doi.org/10.1103/PhysRev.87.835

[26] Crowell, C. R., & Sze, S. M. (1966). Current transport in metal-semiconductor barriers. Solid-state electronics, 9(11-12), 1035-1048. https://doi.org/10.1016/0038-1101(66)90127-4

[27] Ng, K. K., & Sze, S. M. (2007). Physics of semiconductor devices. Hoboken, NJ: Wiley-Interscience. https://doi.org/10.1002/0470068329

Funding

The authors declare that no funds, grants, or other support were received during the preparation of this manuscript.